

Plasmonically Enhanced Thermal Radiation by Means of Surface Phonon Polaritons

Sunmi Shin¹ and Renkun Chen^{2,3,*}

¹*Department of Mechanical Engineering, National University of Singapore, Singapore*

²*Materials Science and Engineering Program, University of California, San Diego, California 92093, USA*

³*Department of Mechanical and Aerospace Engineering, University of California, San Diego, La Jolla, California 92093-0411, USA*



(Received 2 March 2020; revised 19 October 2020; accepted 6 November 2020; published 3 December 2020)

Radiative heat transfer at the nanoscale has the potential to produce thermal emission with both spectral feature and intensity different from the bulk materials. Specifically, the idea of coupling the energy states of photons and phonons using surface phonon polaritons (SPhPs) blurs the boundary between light and heat, opening a path to the manipulation of heat transfer through photonic engineering and breaking the classical limit established by Planck's law. SPhPs can generate a strong energy confinement effect near the surface; however, this effect is only valid within a narrow spectral regime, the so-called reststrahlen band. In this study, we employ a hybrid structure to broaden the effective energy regime for thermal emission by coupling SPhPs and surface plasmon polaritons (SPPs). We report remarkably enhanced thermal emission of a hybrid structure made of a SiO₂ nanoribbon decorated with Au nanoparticles by a factor of 4 over that of a bare SiO₂ nanoribbon. We introduce an experimental technique to quantify the emissivity from the complex nanostructured surface using frequency-dependent heat-transfer measurement. Not only does it enable us to detect feeble emission from a single nanoemitter, but it also differentiates two distinct heat-conducting processes of conduction and radiation, simultaneously. Our work may offer insights to engineer far-field thermal emission using hybrid structures combining the surface plasma and phonon polaritons.

DOI: 10.1103/PhysRevApplied.14.064013

I. INTRODUCTION

Recent efforts to manipulate heat as light have spurred intensive research on radiative heat transfer [1–5]. These “thermal photonics” approaches [6], where “heat meets light” [7], have emerged as useful strategies for a multitude of implications such as radiative cooling [8–15], solar-energy utilization [11,16,17], thermal emissivity modulation [18]. Unlike the traditional concept of heat, which is incandescent, thermal emission via the surface polaritonic resonance arising from the interaction of light and matter is considered a promising approach to effectively utilize thermal energy by converting it into a coherent energy source [1,19]. Because the surface wave can carry the highly confined energy beyond the diffraction limit [20], extensive theoretical and experimental studies have been performed on near-field thermal radiation [2,21–23]. To intensify radiative heat flux, nanogaps smaller than the thermal wavelength (λ_T) have been used to enhance the constructive interference of the evanescent waves from the two opposing surfaces. Sub-100-nm gaps have been experimentally achieved, and the thermally excited surface

wave has been shown to generate strong near-field radiation, breaking the limit of black-body radiation described by Planck's law [2,22–24].

Unlike the evanescent near-field radiation, far-field radiation with nanoscale objects has been generally considered to be far below the black-body limit because the smaller dimension than the skin depth (δ) reduces the capability of absorbing electromagnetic waves, ultimately yielding low emission according to Kirchhoff's law (the so-called volumetric effect [3]). The ability of anisotropic nanostructures to exceed the black-body limit has been recently demonstrated in theoretical and experimental studies within certain angular and spectral ranges by using optical guide modes [3,19,25,26]. In addition, an individual nano-object can maximize the view factor of radiation, or the absorption cross section. In particular, highly anisotropic structures would have a stronger antenna effect, which could potentially yield super-Planckian features in a certain directional and/or spectral range. In our previous work, we showed that long nanoribbon structures of SiO₂ enhanced the emissivity (ε) beyond the thin-film limit via the confined surface energy of SPhPs [19]. ε of individual nano-objects was measured using a sensitive thermometry platform. This quantitative study revealed the

*rkchen@ucsd.edu

contribution of SPhPs in enhancing thermal radiation with anisotropic structures. Importantly, the enhancement by polaritons enables photonic engineering of heat transport through manipulation of the optical properties of the surroundings and emitters. However, the experimental study of nanoemitters for efficient heat transfer remains in the early stage [27,28], and the reported ε of ~ 0.2 , albeit higher than the thin-film value of 0.062 [19], remains much lower than the blackbody limit. To achieve high emission, broadened spectral absorption near the peak of the Planckian distribution as well as high energy confinement to enhance the optical cross-section are required.

It is clearly beneficial to employ surface phonon polaritons (SPhPs) to manipulate radiative heat transfer at room temperature because the dominant thermal wavelength at 300 K (i.e., approximately 10 μm) is located within the reststrahlen band energy regime where SPhPs can be supported. SPhPs have a narrow spectral response within the reststrahlen band bounded by the two resonance frequencies of transverse and longitudinal optical phonons (e.g., ω_{TO} and ω_{LO}). In addition, compared with surface plasmon polaritons (SPPs), SPhPs have low loss near ω_{TO} , which can lead to a high quality (Q) factor of >100 [29,30]. Although implying the selective feature of SPhPs, the

narrow band response and lower imaginary part of the permittivity limit the total energy flux that can be absorbed or emitted from a single object, which is the product of the integration over the entire spectral range. In contrast, SPPs can support a more broadband spectral response owing to the high loss below their characteristic frequency, the so-called surface plasmon frequency ($= \omega_p/\sqrt{2}$, where ω_p is the bulk plasma frequency). However, there is a large discrepancy between ω_p (usually in the UV-vis regime) and the thermal wavelength at room temperature (in the mid-IR regime). For this reason, previous studies reporting a noticeable effect of SPPs on far-field thermal radiation were performed at high temperature [31,32].

In this study, we employ a metal-dielectric hybrid structure to tune the energy-dispersive property at the surface using hybrid modes of SPhPs and SPPs. Specifically, Au NPs with diameters of approximately 50 nm are dispersed on SiO₂ nanoribbons (NRs) (100 nm thickness, 10 μm width, and 400 μm length) as shown in Fig. 1(a). Although the SPP mode itself does not efficiently support the thermal emission in the IR regime owing to disparity in the spectra (visible for Au SPP and mid-IR for thermal emission), the metallic surface of the Au nanoparticles (NPs) allows more localized energy confinement at the SiO₂ surface over the

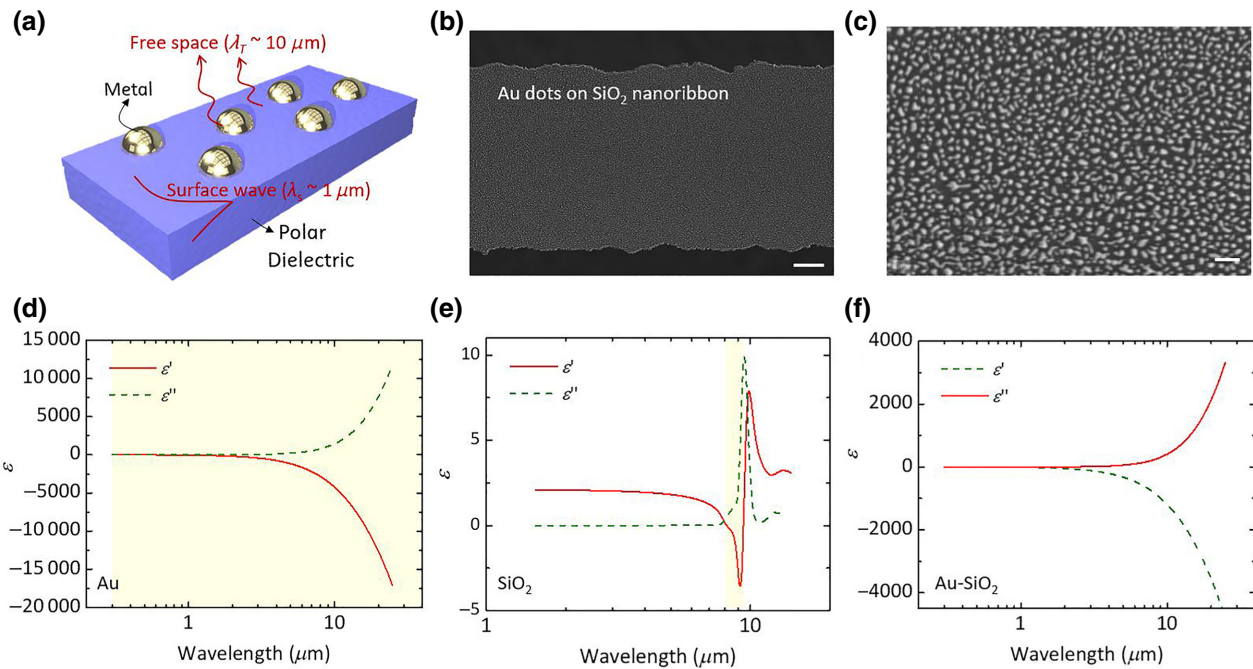


FIG. 1. (a) Schematic illustration of hybrid structure consisting of metal NPs on a polar dielectric NR. (b), (c) SEM images of Au dots deposited on SiO₂ NR. The scale bars correspond to 2 μm and 200 nm for (b) and (c), respectively. The width of the NR is approximately 11.5 μm . Permittivity of Au (d) and SiO₂ (e) as a function of wavelength, where the colored area presents metallic regime. Specifically, the narrow band defined by the Lorentzian distribution in (e) is called the reststrahlen band. (f) Effective permittivity of Au-SiO₂ determined using the effective medium theory, where the volume fraction of 28% and 72% for Au and SiO₂ is applied, respectively.

broader spectral enhancement than the energy dispersion of SiO_2 alone.

Metals and polar dielectrics exhibit different optical properties, as expressed by the Drude and Lorentz models, respectively. Figures 1(d) and 1(e) show the distinct permittivity of Au [33] and SiO_2 [34]. The ω_P of Au corresponds to a wavelength of approximately 300 nm; thus, SPP modes lead to the maximum emittance peak appearing in the UV regime. At frequencies below ω_P , both the real (ϵ') and imaginary (ϵ'') parts of the permittivity monotonically increase [Fig. 1(d)]. The surface modes can still be supported over the broad energy range; however, the high refractive index results in strong reflection at the surface. High reflectance blocks absorption in the emitter and thus reduces the emission enhancement by SPP modes in the IR regime. However, SiO_2 presents two resonant frequencies by optical phonons at approximately 10 μm [8 and 9.5 μm for transverse optical (TO) and longitudinal optical (LO) phonons, respectively], and the two frequencies are closely located. The refractive index becomes zero at the resonant frequencies; thus, the energy dispersion of the polar dielectrics involves sharp transitions near the boundary of the reststrahlen band, as observed for the permittivity of SiO_2 [Fig. 1(e)]. Evidently, SPPs and SPhPs have highly dissimilar energy dispersions. However, the use of hybrid structures with hybridized SPPs and SPhPs is another strategy to manipulate the energy dispersion and engineer the thermal emission.

The hybrid structures also possess an additional challenge for extracting the thermal emissivity. In our previous work, we introduced a measurement platform to quantify ϵ of SiO_2 NRs [19]. The value of ϵ was extracted by measuring the effective thermal conductivity of NRs with various lengths via a thermal fin model. The length-dependent measurement requires negligible variation of the material properties (namely, the thermal conductivity κ and emissivity ϵ) of multiple samples to enable the extraction of a single ϵ value. Amorphous SiO_2 possesses a bulklike κ even at the nanoscale because of the short phonon mean free path [35,36]. However, unlike the pure SiO_2 NR we studied earlier [19], thermal conductivity of the present hybrid structures is not known and could vary for specimens with different lengths, due to the possible morphological difference of the annealed Au NPs. Because it is difficult to prepare identical Au structures for a length-dependent study, in this work, we also develop a heat-transfer measurement platform in the frequency domain, in which the thermal penetration depth, rather than the physical specimen length, is varied to extract the thermal emissivity of a single NR sample based on the fin model. This methodology enables the characterization of ϵ from a single specimen, without resorting to samples of variable length. In addition, the platform allows us to determine κ and ϵ simultaneously and thus does not require knowledge of the thermal conductivity.

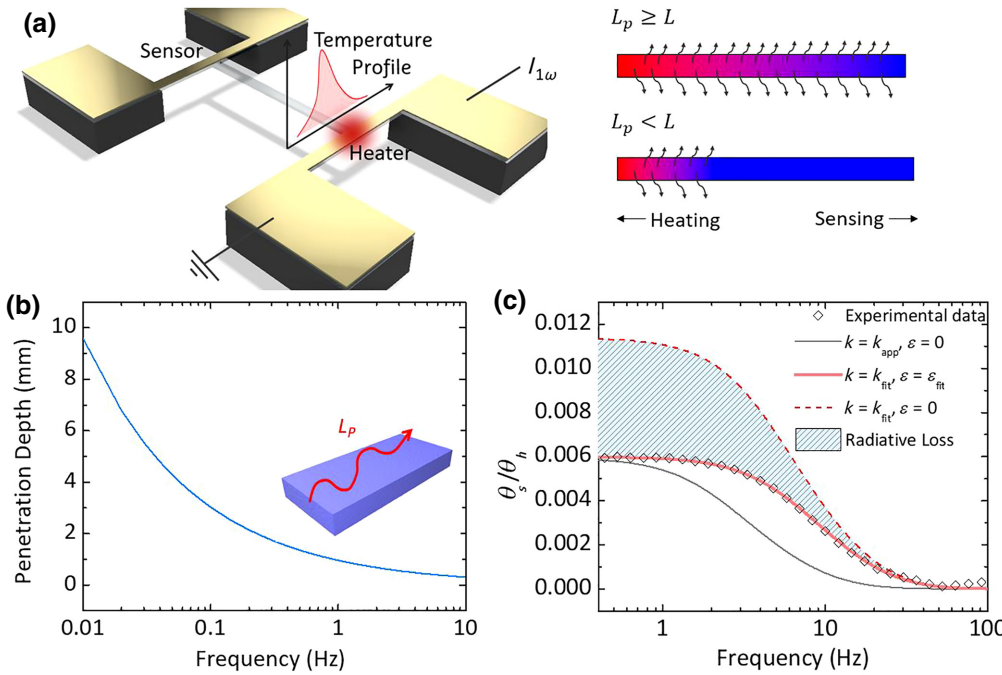
II. METHODS

A. Device fabrication

To measure thermal emissivity from SiO_2 NRs coated with Au NPs, we fabricate suspended microdevices integrated with the NRs. The fabrication process is similar to our previous studies on bare SiO_2 NR and amorphous Si NR [19,37]. A 100-nm thermal oxide film on a Si wafer is prepared. Metal beams with Ti/Pt (80 nm in thickness) are patterned on top of the SiO_2 layer using lithographic patterning followed by anisotropic plasma etching and isotropic XeF_2 etching to fabricate the suspended platform. The width and length of the SiO_2 NRs are defined by the photolithography process. The resultant NRs have a width of approximately 11.5 μm . Then, Au is sputtered for a very short time (5 s) to ensure that the Au layer is discontinuous. Finally, we anneal the device at 200 °C for 12 h, which results in further aggregation of the Au layer and the generation of Au NPs, as shown in the electron micrographs in Figs. 1(b) and 1(c).

B. Thermal transport measurement scheme to extract thermal emissivity

We develop a measurement scheme to extract thermal emissivity of single nanoribbons coated with Au NPs. The scheme is schematically shown in Fig. 2, with additional details shown in Note S1 and Fig. S1 within the Supplemental Material for the heat-transfer model [38]. As shown in Fig. 2(a), the two metal beams on the suspended devices are used as the heater and thermometry, with the sample (emitter) placed across the two beams. By suspending the heating beam and connecting it to the NR, we can use an ac current [$I(\omega)$] to heat up the beam with its peak temperature rise in the middle of the beam, as illustrated in Fig. 2(a). The hybrid structure emitter with hybrid Au/ SiO_2 is placed across the two suspended metal beams [Fig. 2(a)]. We probe the temperature rise at the sensing beam (θ_s) by measuring the resistance change of the metal beams, with precalibrated temperature coefficient of resistance (TCR). In this study, we use a thin Pt layer (approximately 80 nm) with an adhesive Ti layer for both the sensing and heating beams. Heat transport along the ribbon is dominated by radiation and conduction. Convection heat transfer is negligible because of the high vacuum level of the enclosed measurement chamber (approximately 10⁻⁶ Torr). The temperature rise at the heating side (θ_h) is measured by detecting the 3 ω voltage, corresponding to the second harmonic component of the temperature rise (i.e., the well-known 3 ω method [39]), and the ac modulated heating results in a high measurement sensitivity against dc thermal noise. Similarly, the sensing-side temperature rise (θ_s) is measured by detecting an oscillating voltage, the 2 ω voltage, by applying dc current. The details of this measurement are reported in



our previous study [19,40], but here we extend it to extract thermal emission of single nanoribbons by considering both heat conduction and radiation in the ribbon.

The approach to extract the emissivity is to vary the thermal penetration depth (L_p) by modulating the ac heating current at angular frequency ω (heat flux modulated at 2ω):

$$L_p = \sqrt{\frac{\alpha}{2\omega}} = \sqrt{\frac{\kappa}{2\rho C\omega}}, \quad (1)$$

where α , κ , ρ , and C are thermal diffusivity, thermal conductivity, density, and specific heat capacity, respectively. As shown in Figs. 2(a) and 2(b), in the low-frequency regime, where L_p becomes much longer than the NR sample length (L), the radiative heat loss will be present over the entire sample length. Upon increasing the heating frequency, L_p is reduced, which decreases the effective length and surface area to contribute to radiation. The controlled-frequency study works as an alternative approach to effectively change the relative contributions of heat conduction and thermal radiation, as we achieved by varying the physical length of the specimen in our earlier work [19].

We model the heat-transfer process in the NR specimen and the metal beams with the consideration of the radiation heat loss from the NR. We consider the heat-transfer fin model in the NR in the time domain as

$$\frac{\partial\theta(x,t)}{\partial t} = \alpha \frac{\partial^2\theta}{\partial x^2} - \frac{hP}{\rho CA}\theta, \quad (2)$$

where θ is the temperature ($= T - T_0$, with T_0 being the ambient temperature), h is the radiative heat-transfer coefficient ($= 4\varepsilon\sigma\theta^3$), P and A are the perimeter and the cross-section area of the NR. The schematic of the heat-transfer

FIG. 2. Schematic illustration of measurement platform (a) and thermal penetration depth (L_p) relative to the length of the nanoribbon (L). (b) Plot of penetration depth as a function of heating frequency. (c) Plot of temperature rise ratio between the sensing and heating sides with experimental data (symbols) and fitted results (lines), where the shaded area indicates the effect of radiative loss.

model is shown in detail in Fig. S1 within the Supplemental Material [38]. For a modulated temperature rise with the angular frequency ω , namely, $\theta(x, t) = \theta(x)e^{j\omega t}$, the ratio of the temperature rises between the heating and sensing beams can be determined (see Note S1 within the Supplemental Material for a detailed derivation [38]):

$$\frac{\theta_s}{\theta_h} = \frac{1}{\frac{\kappa_1 A_1 a_1}{\kappa_2 A_2 a_2} \frac{\sinh(a_2 L_2)}{\tanh(a_1 L_1)} + \cosh(a_2 L_2)}, \quad (3)$$

where L is the length, $i = 1, 2$ for the heating beam and the NR specimen, respectively, and

$$(a_1)^2 = \frac{j\omega}{\alpha_1^2}, \quad (4)$$

$$(a_2)^2 = \frac{j\omega}{\alpha_2^2} + \frac{h_2 P_2}{\kappa_2 A_2}. \quad (5)$$

As shown in Fig. 2(c), we detect the temperature rise in the heater and sensor with the modulated Joule heating scheme. The experimentally determined temperature rise ratios (θ_s/θ_h) are fitted with the modeled results obtained using Eq. (3). In Fig. 2(c), the solid lines are the fitted curves, and the results overlap well with the experimental data [symbols in Fig. 2(c)].

C. Modeling

To study the energy-dispersive property of the hybrid structures, we model the dispersion relations of various surface structures using a finite-element method (COMSOL

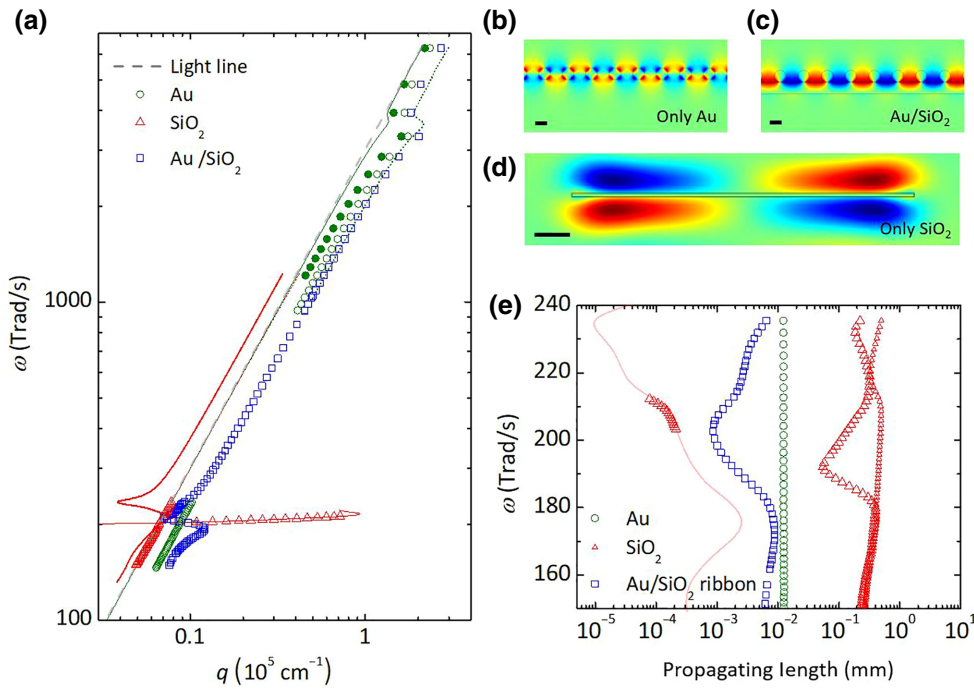


FIG. 3. (a) Plots of energy dispersions of Au nanoparticles (NPs), a bare SiO_2 nanoribbon (NR), and a hybrid SiO_2 NR with Au NPs, corresponding to the legends of Au, SiO_2 , and Au/SiO_2 , respectively. Symbols are modeling results on Au NPs and SiO_2 or hybrid Au/ SiO_2 NRs (width = 10 μm) from the finite-element simulations using COMSOL and the solid lines are analytical modeling results on SiO_2 or Au thin films (with infinite lateral dimensions). (b)–(d) Magnetic field images for the Au NPs (b), the hybrid Au- SiO_2 , (c) and the SiO_2 NR (d) surfaces at 9 and 9.15 μm , respectively. (e) Plot of the calculated propagating lengths in the three structures: Au NP array, pure SiO_2 NR, SiO_2 NR with Au NP array.

Multiphysics). The equations used in the model are shown in Note S2 within the Supplemental Material [38]. The anisotropic three-dimensional structures with high aspect ratios require extensive numerical calculation. Here, we employ two-dimensional modeling to understand the physical mechanisms. We numerically calculate three cases in the model: (i) a SiO_2 NR with 10 μm width and infinite length; (ii) a Au NP array only; (iii) the same SiO_2 NR coated with Au NPs on top (hybrid Au/ SiO_2). The modeling results are shown in Fig. 3 and are discussed in the next section.

III. RESULTS AND DISCUSSION

A. Modeling results

The modeling results of the various nanoribbons (Au, SiO_2 , and Au/SiO_2) are shown as symbols in Fig. 3(a), along with the solid lines representing the analytical modeling results of thin films of SiO_2 and Au, both with 100 nm thickness and infinite lateral dimensions. As expected, the infinite Au and SiO_2 films induced the confined surface modes with a peak in the propagating vector, q , in the UV-vis (3500 Trad/s) and IR (200 Trad/s) regimes, respectively. The SiO_2 film has the much higher peak intensity but narrower effective energy range in the SPhPs compared to SPPs in the Au film. Interestingly, the hybrid Au/ SiO_2 layer effectively combined the two different features from the SPP and SPhP modes. The hybrid mode sustained the peaks near the resonant frequencies of both modes, and more importantly, the confined dispersion in the IR regime by the SPhPs is broadened. Thus, we can expect enhanced

spectral emittance over the broader mid-IR range, thereby increasing ε .

Furthermore, introducing the Au NPs on top of SiO_2 NR enables the localization of the electromagnetic waves at the surface in the broadened energy regime. For instance, the Au NPs introduced a highly reflective surrounding (e.g., $n \sim 10$ for Au at the 10- μm wavelength) on the SiO_2 surface. Figures 3(b)–3(d) present cross-section views of the ribbon structures and the polarization configurations of the magnetic field for Au, Au/ SiO_2 , and SiO_2 , respectively. The presence of the Au NPs leads to the cavitylike feature, resulting in a stronger localized effect [Figs. 3(b) and 3(c)]. The magnetic and electric field images in Fig. S3 and Fig. S4, respectively, within the Supplemental Material [38] further demonstrate the coexistence of two periods of polarization, determined by each polar dielectric and metal surfaces. The increase in the field intensity at the SiO_2 surface is accompanied by the reduction of the propagating length [Fig. 3(e)]. Notably, although ε of the bare Au is almost zero because of the strong reflection, it can be used to support efficient emission of SiO_2 in the IR regime due to the strong localization effect. This strong field intensity enhancement effect is also expected to increase the absorption and hence the emittance. Finally, we examine the effect of random (nonperiodic) spatial distribution of the Au NPs on the energy dispersions (see Fig. S5 within the Supplemental Material [38]), which more closely represents our experiment. The results show that while the dispersions with periodic and random Au arrays are not identical, they are generally similar to each other. This is because the characteristic size of the Au nanostructures,

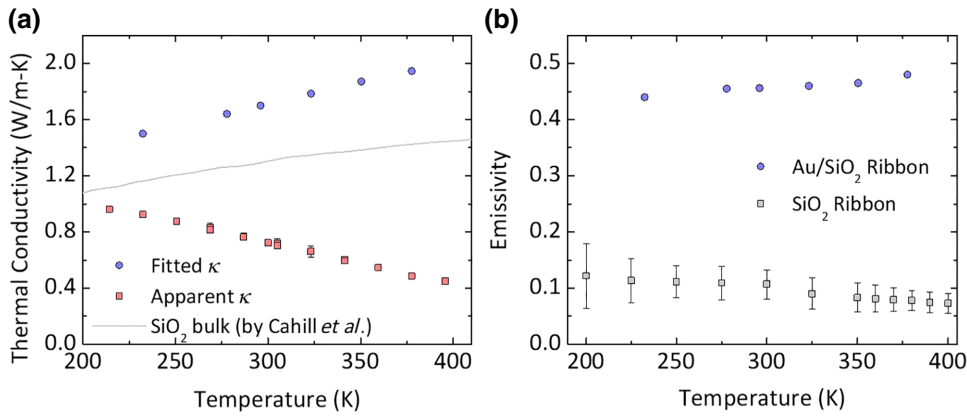


FIG. 4. Plots of apparent and fitted thermal conductivity (a) and emissivity (b) of the 400- μm -long and 11.5- μm -wide Au/SiO₂ nanoribbon. The apparent thermal conductivity (κ_{app}) is determined from Eq. (6), and is used to extract the actual thermal conductivity and emissivity by fitting to the frequency-dependent thermal response [θ_s/θ_h , see Fig. 2(c) and Eq. (3)]. The thermal conductivity of bulk amorphous SiO₂ in (a) is from Cahill [39]. The emissivity of the bare 11.5- μm -wide SiO₂ nanoribbon is from our earlier study [19].

including their diameter and spacing, is much smaller than the thermal wavelength (approximately 10 μm).

B. Measured thermal emissivity and conductivity

Unlike the bare SiO₂ NRs we study earlier [19], which possess constant bulklike thermal conductivity at the nanoscale, the randomly distributed Au NPs on SiO₂ make it difficult to ensure identical κ across specimens of multiple lengths to extract ε . To characterize two unknown parameters (e.g., κ and ε) simultaneously from one single specimen, we measure and analyze the ratios between the sensing and heat beam temperatures (θ_s/θ_h) at various heating frequencies, which controls L_p [Eq. (1)]. We measure θ_s , θ_h , and θ_s/θ_h of the hybrid NR sample from 200 to 400 K (see Fig. S2 within the Supplemental Material for the raw data [38]). By fitting the θ_s/θ_h data using Eq. (3) at each temperature [similar to the one shown in Fig. 2(c) at room temperature], we can determine both the thermal conductivity (κ) and thermal emissivity (ε) of the NR. Figure 4 presents the fitted results of κ and ε as a function of temperature for the hybrid SiO₂/Au NR with width of 11.5 μm . Also shown in Fig. 4(a) is the apparent thermal conductivity (κ_{app}), which is determined in the low-frequency regime, where the θ_s/θ_h is plateaued, as

$$\frac{\theta_s}{\theta_h} = \frac{G_{\text{app}}}{G_{\text{beam}} + G_{\text{app}}}, \quad (6)$$

$$G_{\text{app}} = \kappa_{\text{app}} \frac{A_c}{L}, \quad (7)$$

where G_{app} and G_{beam} are the apparent and beam thermal conductance, respectively. In the absence of radiative heat loss, κ_{app} will be the intrinsic κ of the NR specimen. However, our specimens have a significant radiation heat-loss

effect, which can be comparable to heat conduction along the specimen at certain modulation frequency ω . Radiative heat loss reduces κ_{app} due to the exponential decay of the temperature while heat is transferred along the NR specimen from the heater to the sensor. The degree of this exponential reduction is measured by a_2 , as described in Eqs. (3) and (5). Hence, we observe a larger deviation between κ_{app} and κ at higher temperature, as shown in Fig. 4(a), suggesting an increasing radiation heat loss, as expected. Figure 4(a) compares κ of the NR with the bulk κ of amorphous SiO₂. The presence of Au NPs leads to a slight increase in κ compared to bulk SiO₂, however, because of the discontinuous feature of the Au layer [shown in Fig. 1(c)], the value of κ remains close to that of SiO₂.

Figure 4(b) shows the extracted ε of the Au/SiO₂ emitter, along with that of the bare SiO₂ NR sample without the Au NPs. The hybrid Au/SiO₂ emitter exhibits a considerably higher value of 0.46 at 300 K, which is about a factor of 4 compared to that of the bare SiO₂ sample of the same dimension ($\varepsilon = 0.11$ with 11.5- μm -wide bare SiO₂ ribbons at 300 K [19]). This significant enhancement of the emissivity is the result of the coupled SPP and SPhP effects that modified the SPhP dispersions and the broadening of the resonant spectrum in the mid-IR regime as well as the emergence of the SPP resonance peak in the visible regime, as theoretically analyzed earlier (Fig. 3). The modified resonance features are also manifested in the temperature dependence of the emissivity shown in Fig. 4(b): at higher temperature, the emissivity of the hybrid NR emitter increases while that of the SiO₂ NR decreases, resulting in a greater ratio between the two (about 7 at 375 K). In bare SiO₂ NRs, the emissivity is primarily a result of coherent resonance of SPhP in the mid-IR range in the ribbon structure, as we have studied earlier [19].

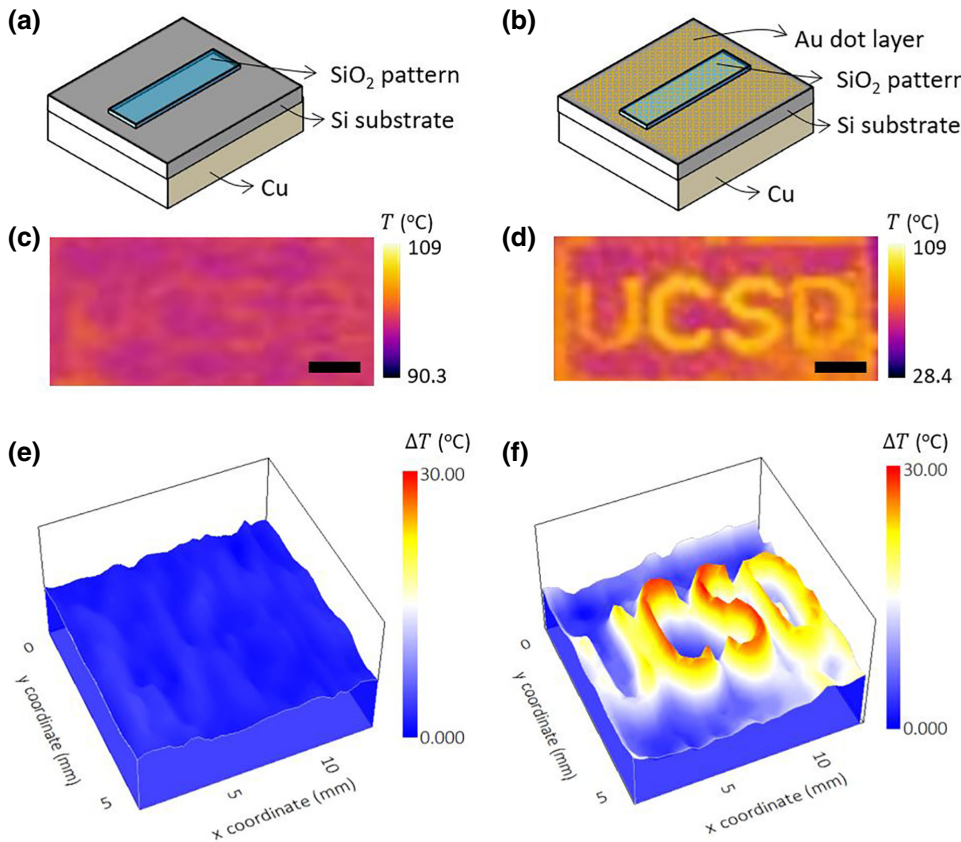


FIG. 5. Schematic illustration of Si substrate patterned with SiO_2 only (a) and with Au/SiO_2 hybrid structure (b). IR thermal imaging of “UCSD” logo patterns made of SiO_2 only (c), (e) and patterns made of Au/SiO_2 hybrid structures (d), (f). Both samples are placed on a 135 °C hot plate, and the temperature scales in the IR images of (e) and (f) are the same. The scale bars in (c), (d) correspond to 2 mm.

This coherent effect is stronger at lower temperature due to the longer lifetime of optical phonons in SiO_2 [41] and consequently the narrower and sharper resonance peaks [19]. Therefore, the emissivity is higher at lower temperature in pure SiO_2 NRs. On the other hand, the Au NPs broaden the mid-IR SPhP resonance also and results in a new SPhP peak in UV-vis [Fig. 3(a) and 3(e)]. Both of these effects are expected to result in higher emissivity at higher temperature.

C. Infrared image of the hybrid structure

To directly visualize the enhanced thermal emissivity of SiO_2 with the Au NPs, we did IR images with patterned SiO_2 structures with and without the Au NPs, schematically shown in Figs. 5(a) and 5(b), respectively. The SiO_2 layer is patterned into the letters “UCSD” using standard photolithography and etching processes. The patterns are prepared on top of a Si wafer substrate sitting on a Cu block to obtain a uniform thermal background. The entire device is placed on a hot plate at 135 °C for thermal imaging. The “UCSD” logo is clearly more visible in Figs. 5(d) and 5(f) with the hybrid structures with the Au nanoparticles than that of the pure SiO_2 pattern [Figs. 5(c) and 5(e)]. This result demonstrates the considerably higher ε at the hybrid structure with the Au nanoparticles.

IV. CONCLUSION

In conclusion, we employ a hybrid structure of the SiO_2 nanoribbon with Au nanoparticles to engineer the energy dispersion of SPhP in the mid-IR regime, therefore enhancing its thermal emissivity (ε) from room to high temperature. To extract the thermal emissivity from the nanoscale emitter, we develop a frequency-domain heat-transfer measurement platform by integrating the emitter with microfabricated heating and sensing beams. The measurement utilizes the modulated heating to vary the thermal penetration depth relative to the nanoribbon length, which enables simultaneous determination of thermal conductivity (κ) and ε from a single ribbon using a thermal fin model. We observe significant enhancement of ε of the hybrid nanoribbon structure by a factor of 4 near room temperature over that of the bare SiO_2 nanoribbon owing to the coupled SPP and SPhP modes. The resultant dispersion possessed a strong confinement effect with shorter propagating length in the mid-IR regime by virtue of the SPhP surface modes; however, the effective energy range is broadened with the presence of Au nanoparticles, which support SPPs in the UV-vis range, and thus enhance the ε . This work provides a pathway to enhance far-field thermal radiation in nanoscale emitters featured with plasmon and phonon polaritons.

ACKNOWLEDGMENTS

The authors acknowledge support from the National Science Foundation (DMR #1508420 and #2005181). Device fabrication is performed at the San Diego Nanotechnology Infrastructure (SDNI) of UCSD, a member of the National Science Foundation (Grant No. ECCS-1542148). S.S. acknowledges support from MOE startup, Singapore (R-265-000-679-133).

- [1] J. J. Greffet, R. Carminati, K. Joulain, J. P. Mulet, S. Main-guy, and Y. Chen, Coherent emission of light by thermal sources, *Nature* **416**, 61 (2002).
- [2] B. Song, D. Thompson, A. Fiorino, Y. Ganjeh, P. Reddy, and E. Meyhofer, Radiative heat conductances between dielectric and metallic parallel plates with nanoscale gaps, *Nat. Nanotechnol.* **11**, 509 (2016).
- [3] V. A. Golyk, M. Kruger, and M. Kardar, Heat radiation from long cylindrical objects, *Phys. Rev. E Stat. Nonlin. Soft Matter. Phys.* **85**, 046603 (2012).
- [4] J. Ordóñez-Miranda, L. Tranchant, T. Tokunaga, B. Kim, B. Palpant, Y. Chalopin, T. Antoni, and S. Volz, Anomalous thermal conductivity by surface phonon-polaritons of polar nano thin films due to their asymmetric surrounding media, *J. Appl. Phys.* **113** (2013).
- [5] B. Liu, W. Gong, B. Yu, P. Li, and S. Shen, Perfect thermal emission by nanoscale transmission line resonators, *Nano Lett.* **17**, 666 (2017).
- [6] S. H. Fan, Thermal photonics and energy applications, *Joule* **1**, 264 (2017).
- [7] S. V. Boriskina, J. K. Tong, W. C. Hsu, B. L. Liao, Y. Huang, V. Chiloyan, and G. Chen, Heat meets light on the nanoscale, *Nanophotonics-Berlin* **5**, 134 (2016).
- [8] Y. C. Peng, J. Chen, A. Y. Song, P. B. Catrysse, P. C. Hsu, L. L. Cai, B. F. Liu, Y. Y. Zhu, G. M. Zhou, D. S. Wu *et al.*, Nanoporous polyethylene microfibres for large-scale radiative cooling fabric, *Nat. Sustain.* **1**, 105 (2018).
- [9] Z. Chen, L. X. Zhu, A. Raman, and S. H. Fan, Radiative cooling to deep sub-freezing temperatures through a 24-h day-night cycle, *Nat. Commun.* **7**, 13729 (2016).
- [10] P. C. Hsu, A. Y. Song, P. B. Catrysse, C. Liu, Y. C. Peng, J. Xie, S. H. Fan, and Y. Cui, Radiative human body cooling by nanoporous polyethylene textile, *Science* **353**, 1019 (2016).
- [11] L. X. Zhu, A. P. Raman, and S. H. Fan, Radiative cooling of solar absorbers using a visibly transparent photonic crystal thermal blackbody, *P. Natl. Acad. Sci. USA* **112**, 12282 (2015).
- [12] A. P. Raman, M. A. Anoma, L. X. Zhu, E. Rephaeli, and S. H. Fan, Passive radiative cooling below ambient air temperature under direct sunlight, *Nature* **515**, 540 (2014).
- [13] Y. Zhai, Y. G. Ma, S. N. David, D. L. Zhao, R. N. Lou, G. Tan, R. G. Yang, and X. B. Yin, Scalable-manufactured randomized glass-polymer hybrid metamaterial for daytime radiative cooling, *Science* **355**, 1062 (2017).
- [14] T. Li, Y. Zhai, S. M. He, W. T. Gan, Z. Y. Wei, M. Heidarinejad, D. Dalgo, R. Y. Mi, X. P. Zhao, J. W. Song *et al.*,

- A radiative cooling structural material, *Science* **364**, 760 (2019).
- [15] J. L. Kou, Z. Jurado, Z. Chen, S. H. Fan, and A. J. Minnich, Daytime radiative cooling using near-black infrared emitters, *ACS Photonics* **4**, 626 (2017).
- [16] Y. X. Yeng, M. Ghebrebrhan, P. Bermel, W. R. Chan, J. D. Joannopoulos, M. Soljacic, and I. Celanovic, Enabling high-temperature nanophotonics for energy applications, *P. Natl. Acad. Sci. USA* **109**, 2280 (2012).
- [17] P. F. Li, B. A. Liu, Y. Z. Ni, K. K. Liew, J. Sze, S. Chen, and S. Shen, Large-Scale nanophotonic solar selective absorbers for high-efficiency solar thermal energy conversion, *Adv. Mater.* **27**, 4585 (2015).
- [18] A. Krishna, J. M. Kim, J. Leem, M. C. Wang, S. Nam, and J. Lee, Ultraviolet to Mid-infrared emissivity control by mechanically reconfigurable graphene, *Nano Lett.* **19**, 5086 (2019).
- [19] S. Shin, M. Elzouka, R. Prasher, and R. Chen, Far-field coherent thermal emission from polaritonic resonance in individual anisotropic nanoribbons, *Nat. Commun.* **10**, 1377 (2019).
- [20] D. K. Gramotnev and S. I. Bozhevolsky, Plasmonics beyond the diffraction limit, *Nat. Photonics* **4**, 83 (2010).
- [21] B. Song, A. Fiorino, E. Meyhofer, and P. Reddy, Near-field radiative thermal transport: From theory to experiment, *AIP Adv.* **5**, 053503 (2015).
- [22] S. Shen, A. Narayanaswamy, and G. Chen, Surface phonon polaritons mediated energy transfer between nanoscale gaps, *Nano Lett.* **9**, 2909 (2009).
- [23] A. Fiorino, D. Thompson, L. Zhu, B. Song, P. Reddy, and E. Meyhofer, Giant enhancement in radiative heat transfer in sub-30 nm gaps of plane parallel surfaces, *Nano Lett.* **18**, 3711 (2018).
- [24] K. Kim, B. Song, V. Fernández-Hurtado, W. Lee, W. Jeong, L. Cui, D. Thompson, J. Feist, M. H. Reid, and F. J. García-Vidal, Radiative heat transfer in the extreme near field, *Nature* **528**, 387 (2015).
- [25] V. Fernandez-Hurtado, A. I. Fernandez-Dominguez, J. Feist, F. J. Garcia-Vidal, and J. C. Cuevas, Super-Planckian far-field radiative heat transfer, *Phys. Rev. B* **97**, 045408 (2018).
- [26] D. Thompson, L. Zhu, R. Mittapally, S. Sadat, Z. Xing, P. McArdle, M. M. Qazilbash, P. Reddy, and E. Meyhofer, Hundred-fold enhancement in far-field radiative heat transfer over the blackbody limit, *Nature* **561**, 216 (2018).
- [27] J. C. Cuevas, Thermal radiation from subwavelength objects and the violation of Planck's law, *Nat. Commun.* **10**, 3342 (2019).
- [28] J. C. Cuevas and F. J. García-Vidal, Radiative heat transfer, *ACS Photonics* **5**, 3896 (2018).
- [29] M. Tamagnone, A. Ambrosio, K. Chaudhary, L. A. Jaurégui, P. Kim, W. L. Wilson, and F. Capasso, Ultra-confined mid-infrared resonant phonon polaritons in van der waals nanostructures, *Sci. Adv.* **4**, eaat7189 (2018).
- [30] J. D. Caldwell, O. J. Glembocski, Y. Francescato, N. Sharac, V. Giannini, F. J. Bezires, J. P. Long, J. C. Owrusky, I. Vurgaftman, and J. G. Tischler, Low-loss, extreme sub-diffraction photon confinement via silicon carbide localized surface phonon polariton resonators, *Nano Lett.* **13**, 3690 (2013).

- [31] S. Ingvarsson, L. Klein, Y. Y. Au, J. A. Lacey, and H. F. Hamann, Enhanced thermal emission from individual antenna-like nanoheaters, *Opt. Express* **15**, 11249 (2007).
- [32] Y. Y. Au, H. S. Skulason, S. Ingvarsson, L. J. Klein, and H. F. Hamann, Thermal radiation spectra of individual subwavelength microheaters, *Phys. Rev. B* **78**, 085402 (2008).
- [33] R. L. Olmon, B. Slovick, T. W. Johnson, D. Shelton, S.-H. Oh, G. D. Boreman, and M. B. Raschke, Optical dielectric function of gold, *Phys. Rev. B* **86**, 235147 (2012).
- [34] J. Kischkat, S. Peters, B. Gruska, M. Semtsiv, M. Chashnikova, M. Klinkmüller, O. Fedosenko, S. Machulik, A. Aleksandrova, and G. Monastyrskyi, Mid-infrared optical properties of thin films of aluminum oxide, titanium dioxide, silicon dioxide, aluminum nitride, and silicon nitride, *Appl. Opt.* **51**, 6789 (2012).
- [35] J. M. Larkin and A. J. McGaughey, Thermal conductivity accumulation in amorphous silica and amorphous silicon, *Phys. Rev. B* **89**, 144303 (2014).
- [36] L. Yang, Q. Zhang, Z. Cui, M. Gerboth, Y. Zhao, T. T. Xu, D. G. Walker, and D. Li, Ballistic phonon penetration depth in amorphous silicon dioxide, *Nano Lett.* **17**, 7218 (2017).
- [37] S. Kwon, J. Zheng, M. C. Wingert, S. Cui, and R. Chen, Unusually high and anisotropic thermal conductivity in amorphous silicon nanostructures, *ACS Nano* **11**, 2470 (2017).
- [38] See Supplemental Material at <http://link.aps.org/supplemental/10.1103/PhysRevApplied.14.064013> for detailed heat-transfer and EM modeling, mode analysis, and energy dispersions with nonperiodic Au nanostructures.
- [39] D. G. Cahill, Thermal conductivity measurement from 30 to 750 K: The 3ω method, *Rev. Sci. Instrum.* **61**, 802 (1990).
- [40] J. Zheng, M. C. Wingert, J. Moon, and R. Chen, Simultaneous specific heat and thermal conductivity measurement of individual nanostructures, *Semicond. Sci. Technol.* **31**, 084005 (2016).
- [41] A. S. Pine and P. E. Tannenwald, Temperature dependence of Raman linewidth and shift in alpha-quartz, *Phys. Rev.* **178**, 1424 (1969).